Formation of a Continuous Solid-Solution Particle and its Application to Rechargeable Lithium Batteries

Hyung-Joo Noh, Seung-Taek Myung, Hun-Gi Jung, Hitoshi Yashiro, Khalil Amine, and Yang-Kook Sun**

High-energy electrode materials are under worldwide development for rechargeable lithium batteries to be used in electric vehicles and other energy storage applications. High capacity and energy density are readily achievable using Ni-rich $Li[Ni_{1-x}M_x]O_2$ (x = 0.1–0.2, M = Ni, Co, Mn, and Al) cathodes. Unfortunately, their structural instability is associated with severe capacity fading on cycling, which hinders practical applications. Here, a method is presented for producing a continuous compositional change between $Li[Ni_{0.8}Co_{0.2}]O_2$ (center) and $Li[Ni_{0.8}Co_{0.01}Mn_{0.19}]O_2$ (surface) in a spherical particle, resulting in an average composition of $Li[Ni_{0.8}Co_{0.06}Mn_{0.14}]O_2$. The chemical composition in the particle is gradually altered by decreasing the Co concentration while adding Mn content. The Ni content remains fixed. Coin cells with the solid-solution cathode deliver a specific capacity over 210 mAh g^{-1} in the voltage range of 2.7–4.3 V vs. Li/Li^+ with capacity retention of 85% over 100 cycles at 25 and 55 °C. The main exothermic temperature upon heating appears at around 250 °C with relatively low heat generation (810 J g^{-1}). The presence of the tetravalent Mn at the particle surface is mainly responsible for the high capacity upon cycling and excellent thermal properties.

1. Introduction

Lithium-ion batteries are the leading power sources for portable electronic devices and are being considered for use in electric vehicles, hybrid electric vehicles, and other energy storage systems. Batteries that satisfy the high energy density, long cycle life, and good thermal stability for the above applications have yet to be developed. To reach that goal, systematic in-situ studies are needed on the structural changes in the electrode materials during charge-discharge cycling, aging, and thermal disintegration.[1]

Nickel-rich cathode materials, such as $Li[Ni_{1-x}M_x]O_2$ ($x \leq 0.2$ and M = Co and Mn), are known to deliver high capacity of 200 mAh g^{-1}.[2] However, the unstable structure at the highly delithiated state gives rise to reaction with the organic electrolyte and carbon anode, causing severe safety problems.[3] A great deal of research has been conducted to eliminate such catastrophic effects by developing flame-retardant additives, thermally stable anodes, and thermally stable cathodes.[4–7] One of the most effective ways to address the safety concern is to coordinate the Ni-rich materials with tetravalent Mn-containing oxide materials, like $Li[Ni_{1/2}Mn_{1/2}]O_2$ or $Li[Ni_{1/3}Co_{1/3}Mn_{1/3}]O_2$, by forming a core-shell particle or a core-shell particle with concentration gradient in the shell.[8–10] Cathode materials with such particle structures have successfully accomplished reversibly high capacity, over 180 mAh g^{-1}, with excellent capacity retention and reliable safety properties. These findings suggest that the physical and chemical states of the particle surface are the crucial factor to significantly change the overall material properties.

Tomograms of these core-shell and core-shell concentration gradient particles revealed that $Li[Ni_{0.8}Co_{0.1}Mn_{0.1}]O_2$ appeared only in the core, and the delivered capacity was mainly due to the core because the outer shell usually possesses the rate-limiting properties (poor Li^+ diffusion).[8–10] It was anticipated that, if the higher concentration of Ni can be maintained from the particle center to the surface, and at the same time the outer surface can be modified by tetravalent Mn, the resulting capacity can be further improved compared to the above two

---

H.-J. Noh, H.-G. Jung, Prof. Y.-K. Sun
Department of WCU Energy Engineering
Department of Chemical Engineering
Hanyang University
Seoul 133-791, South Korea
E-mail: yksun@hanyang.ac.kr

Prof. S.-T. Myung
Department and Institute of Nano Engineering
Sejong University
Seoul 143-747, South Korea

Prof. H. Yashiro
Department of Chemical Engineering
Iwate University
4-3-5 Ueda, Morioka, Iwate 020-8551, Japan

Dr. K. Amine
Chemical Sciences and Engineering Division
Argonne National Laboratory
9700 South Cass Avenue, Lemont, IL 60439, USA
E-mail: amine@anl.gov

DOI: 10.1002/adfm.201200699

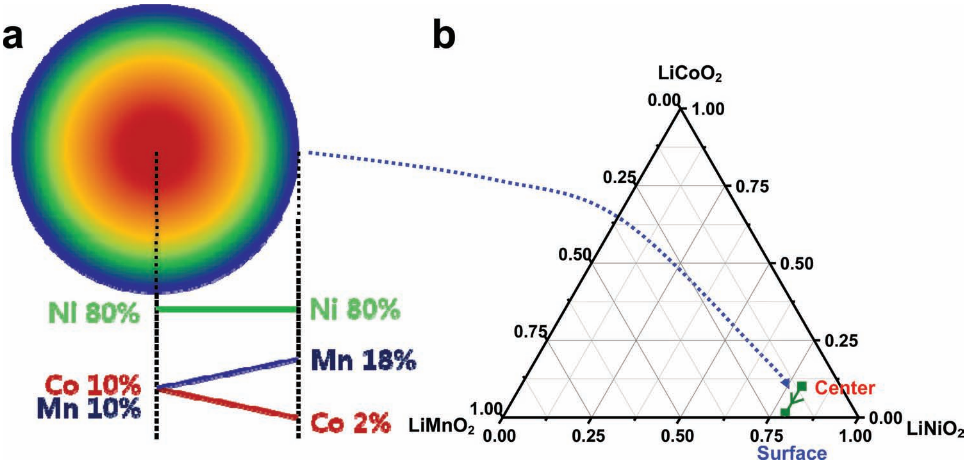

Figure 1. a) Schematic drawing solid-solution particle and b) the resulting phase diagram showing continuous variation in composition, represented by the tie line of Li[$Ni_{0.8}Co_{0.1}Mn_{0.1}$]O_2 (center part) to Li[$Ni_{0.8}Co_{0.02}Mn_{0.18}$]$O_2$ (surface part).

concepts. In addition, the tetravalent Mn in the surface part is responsible for the satisfactory thermal properties. **Figure 1** represents the above hypothesis schematically: i) high concentration of Ni (80%) is maintained throughout the spherical particle and ii) the Co content at the center (10%) is gradually reduced to the outer surface (2%), but Mn replaces the reduced Co content, forming a solid solution in the particle. A prerequisite for the formation of a solid solution in the particle is that it should be spherical.

2. Results and Discussion

2.1. Particle Characterization

Coprecipitation is an effective method for growing a hydroxide seed to a spherical particle with a diameter over 10 µm, as reported earlier.[14] For particle fabrication (see also Experimental Section), a Ni-containing aqueous solution was constantly pumped throughout the coprecipitation reaction so that the Ni concentration was kept to 80% for the hydroxide (**Figure 2**a). At the same time, the Co and Mn contents varied linearly from the center (Co-rich but Mn-free) to the surface (Mn-rich but Co-poor) to give a gradual variation in those transition metal concentrations. The chemical composition determined by EPMA line scan was [$Ni_{0.8}Co_{0.2}$]$(OH)_2$ in the center, along with surface composition of [$Ni_{0.8}Co_{0.01}Mn_{0.19}$]$(OH)_2$. These results indicate that the full concentration gradient was obtained from the center to the surface, with varying Co and Mn contents throughout the whole particle.

Different from the core-shell and concentration gradient core-shell hydroxide, thermal lithiation of the full concentration gradient hydroxide at high temperature (750 °C) may give rise to interdiffusion of each transition metal due to the absence of either a core or shell (see inset of SEM cross-section image in Figure 2b). Since the concentration of Ni was constant throughout the particle in the hydroxide, the Ni distributed

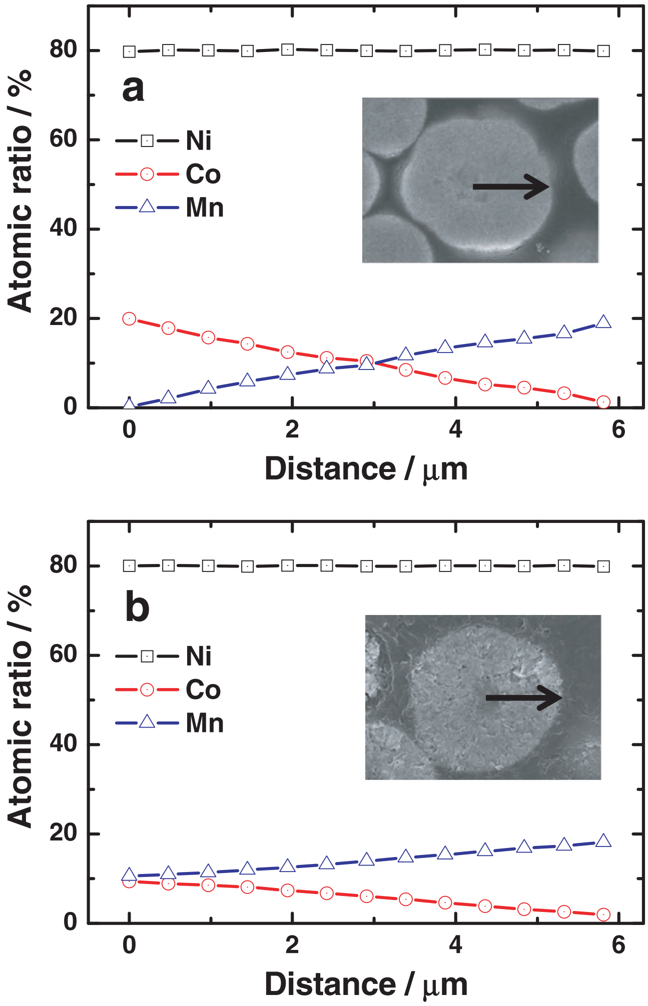

Figure 2. SEM and electron-probe X-ray micro-analysis results for a) SSP [$Ni_{0.8}Co_{0.06}Mn_{0.14}$]$(OH)_2$ and b) SSP Li[$Ni_{0.8}Co_{0.06}Mn_{0.14}$]$O_2$.

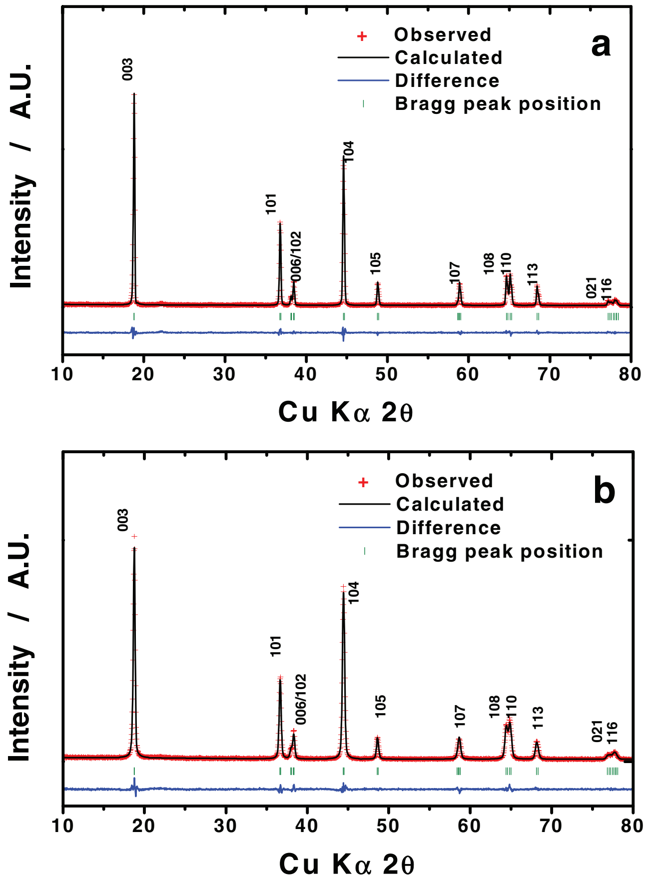

Figure 3. Rietveld refinement results of XRD data for a) $Li[Ni_{0.8}Co_{0.2}]O_2$ and b) $Li[Ni_{0.8}Co_{0.06}Mn_{0.14}]O_2$.

evenly from the center to the surface in the particle after the calcination at high temperature. However, the unusual distribution of Co and Mn (namely, center that is Co-rich and Mn-free, and surface that is Co-poor and Mn-rich) in the hydroxide led to interdiffusion of both elements at the center, giving the chemical composition $Li[Ni_{0.8}Co_{0.1}Mn_{0.1}]O_2$. The concentration of Co gradually declines from the center, and it finally settles down to 2% near the surface. By contrast, the Mn concentration increases linearly, and it reaches 18% at the surface, leading to a chemical composition of $Li[Ni_{0.8}Co_{0.02}Mn_{0.18}]O_2$. Taken together, these results describe a solid solution with a composition between $Li[Ni_{0.8}Co_{0.1}Mn_{0.1}]O_2$ and $Li[Ni_{0.8}Co_{0.02}Mn_{0.18}]O_2$ (see tie line in Figure 1b). The total average composition of the solid solution particle (SSP) was found to be $Li[Ni_{0.8}Co_{0.06}Mn_{0.14}]O_2$, determined by atomic absorption spectroscopy (AAS).

Figure 3 compares powder X-ray diffraction (XRD) patterns of $Li[Ni_{0.8}Co_{0.2}]O_2$ and SSP $Li[Ni_{0.8}Co_{0.06}Mn_{0.14}]O_2$. The as-synthesized $Li[Ni_{0.8}Co_{0.2}]O_2$ exhibited a well-ordered layer structure with $R\bar{3}m$ space group, where there is a clear peak split of (006)/(102) and (108) and (110) pairs. The SSP $Li[Ni_{0.8}Co_{0.06}Mn_{0.14}]O_2$ was also crystallized into the same layer structure. However, compared to the pattern for $Li[Ni_{0.8}Co_{0.2}]O_2$, there is less splitting of the (006)/(102) and (108) and (110) pairs, which is presumably due to the addition of Mn. The behavior is also observed in Mn-doped $LiNi_{1-x}Mn_xO_2$.[11,12] The peak ratio of (003)/(104) is known to be a measure of cation mixing in the layered crystal structure. Because of the gradual change in the chemical composition of the SSP $Li[Ni_{0.8}Co_{0.06}Mn_{0.14}]O_2$, it, indeed, is not possible to refine the crystal structure from the XRD pattern. Since the peak ratio of (003)/(104) is greater for $Li[Ni_{0.8}Co_{0.2}]O_2$ than that of SSP $Li[Ni_{0.8}Co_{0.06}Mn_{0.14}]O_2$, we performed Rietveld refinement of the XRD patterns based on the average chemical composition, $Li[Ni_{0.8}Co_{0.06}Mn_{0.14}]O_2$, measured by chemical analysis. The calculated content of Ni in the Li layer was found to be approximately 1.4% for the $Li[Ni_{0.8}Co_{0.2}]O_2$, whereas the cation mixing for the SSP $Li[Ni_{0.8}Co_{0.06}Mn_{0.14}]O_2$ was found to be 2.8%. As seen from the (003)/(104) peak ratio, a slightly higher level of cation mixing is evident for the SSP $Li[Ni_{0.8}Co_{0.06}Mn_{0.14}]O_2$. Also, the calculated lattice parameters for $Li[Ni_{0.8}Co_{0.06}Mn_{0.14}]O_2$ were slightly greater than those for $Li[Ni_{0.8}Co_{0.2}]O_2$ (**Table 1** and **2**). In particular, the larger *a*-axis indicates variation in the distance between transition metal and oxygen, meaning the average oxidation state of the transition metals changes as the continuous solid solution forms between $Li[Ni_{0.8}Co_{0.1}Mn_{0.1}]O_2$ and $Li[Ni_{0.8}Co_{0.02}Mn_{0.18}]O_2$ in a particle.

The SSP $Li[Ni_{0.8}Co_{0.06}Mn_{0.14}]O_2$ was investigated by X-ray photoelectron spectroscopy (XPS) to examine the chemical state. With this technique consecutive surface etching by Ar^+ ion gives direct information on the chemical state as a function of depth. The outermost surface was etched about 10 Å in depth to eliminate the effect of the air-oxidized passive film. Then, the surface was etched to 1 μm in a direction from the surface toward the particle center. For the Ni XPS spectrum, the main peak was observed at 854.1 eV for the 2p3/2 orbital, which is closer to the binding energy for Ni^{2+} than that for Ni^{3+} (**Figure 4**a). Further etching induced a slight shift of peaks toward higher binding energy for the Ni 2p3/2 and Ni 2p1/2 orbitals (marked as black dashed lines), showing subtle increase in the oxidation state of

Table 1. Rietveld refinement results of XRD patterns for $Li[Ni_{0.8}Co_{0.2}]O_2$.

Formula				$Li[Ni_{0.8}Co_{0.2}]O_2$		
Crystal system				Rhombohedral		
Space group				$R\bar{3}m$		
Atom	Site	*x*	*y*	*z*	*g*	*B* [Å^2]
Li1	3*a*	0	0	1/2	0.986	0.6
Ni2	3*a*	0	0	1/2	0.014(1)	0.6
Ni1	3*b*	0	0	0	0.8	0.7
Co	3*b*	0	0	0	0.2	0.7
O	6*c*	0	0	0.259(2)	1	0.8
a-axis [Å]				2.8633(3)		
c-axis [Å]				14.1602(9)		
Li-O [Å]				2.1080(15)		
M[a] -O [Å]				1.9596(19)		
Unit volume [Å^3]				100.544(11)		
R_{wp} [%]				9.88		
R_p [%]				7.30		

[a] Denotes transition metals Ni and Co.

Table 2. Rietveld refinement results of XRD patterns for $Li[Ni_{0.8}Co_{0.06}Mn_{0.14}]O_2$.

Formula		$Li[Ni_{0.8}Co_{0.06}Mn_{0.14}]O_2$				
Crystal system		Rhombohedral				
Space group		$R\bar{3}m$				
Atom	Site	*x*	*y*	*z*	*g*	*B* [Å^2]
Li1	3*a*	0	0	1/2	0.972	0.5
Ni2	3*a*	0	0	1/2	0.028(2)	0.5
Li2	3*b*	0	0	0	0.028(2)	0.8
Ni1	3*b*	0	0	0	0.772	0.8
Mn	3*b*	0	0	0	0.14	0.8
Co	3*b*	0	0	0	0.06	0.8
O	6*c*	0	0	0.258(3)	1	0.8
a-axis [Å]				2.8737(5)		
c-axis [Å]				14.2129(8)		
Li-O [Å]				2.1114(16)		
M$^{a)}$ -O [Å]				1.9704(22)		
Unit volume [Å^3]				101.645(15)		
R_{wp} [%]				10.5		
R_p [%]				8.51		

$^{a)}$ Denotes transition metals Ni, Co, and Mn.

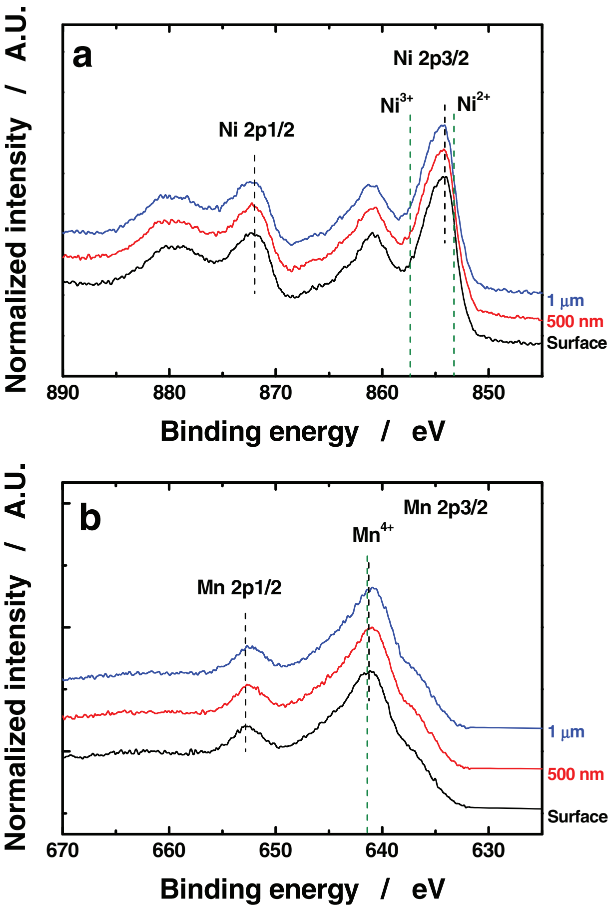

Figure 4. XPS data as a function of particle depth for the SSP $Li[Ni_{0.8}Co_{0.06}Mn_{0.14}]O_2$: a) Ni 2p and b) Mn 2p.

Ni with depth. For the Mn XPS spectrum, the main peak was found at 641.5 eV (marked as black dashed line), which is close to the value for tetravalent Mn (Figure 4b). With etching, the resulting spectra moved to lower binding energy, indicating a lower oxidation state.

By means of the XPS analysis, we observed the chemical states of the spherical SSP $Li[Ni_{0.8}Co_{0.06}Mn_{0.14}]O_2$ changing with depth, from the surface to 1 μm toward the center. As the etching progressed deeper, the Co content increased and the amount of Mn decreased. Because the oxidation state of Co is always trivalent in the layer structured compound (space group $R\bar{3}m$), the variation in oxidation state of Co was excluded. The valence of Ni was lowered with increasing Mn content, reaching a value close to 2+ on the surface (Figure 4a). The observed binding energy for Mn was located near the value for Mn^{4+} at the surface, and the energy value was somewhat lowered as the Mn content decreased with etching. The above findings explain why the formation of a continuous solid solution results in the gradual variation in the oxidation states for Ni and Mn. The XPS investigation also indicates that the presence of Ni^{2+} accounts for the larger lattice parameters in the SSP $Li[Ni_{0.8}Co_{0.06}Mn_{0.14}]O_2$, particularly, the *a*-axis value, since the ionic radius of Ni^{2+} (0.69 Å)[13] is larger than that of Ni^{3+} (0.56 Å).[13]

Both as-synthesized powders exhibit spherical secondary morphology, as shown in **Figure 5**a,b. The particle size was estimated to be approximately 12 μm in diameter. Since the concentration gradient of transition metals is formed during particle growth in the reactor, control and maintance of the spherical morphology are significantly important to ensure the designed chemical composition of the solid-solution particle. The Though the same synthetic procedure was employed, the resulting morphology for the primary particles was somewhat different for the two compositions. Namely, the primary particle size was about 300–400 nm with irregular particle morphology for $Li[Ni_{0.8}Co_{0.2}]O_2$ (Figure 5a), whereas SSP $Li[Ni_{0.8}Co_{0.06}Mn_{0.14}]O_2$ exhibited nanorod-like primary particles with particle size of approximately 300–400 nm in length and 50–60 nm in width (Figure 5b). In an earlier report, rectangular primary particles were frequently observed in $Li[Ni_{1/3}Co_{1/3}Mn_{1/3}]O_2$ and $Li[(Ni_{1/2}Mn_{1/2})_{1-x}Co_x]O_2$.[14–16] Though we need further investigation to understand the formation of this unique morphology, the presence of the nanorod-like primary particles could have a beneficial effect in improving battery performance due to a reduced Li^+ diffusion path. The measured tap density for both products was excellent, 2.3 g cc^{-1}.

2.2. Cell Testing

Coin cell tests were performed using the synthesized powders as the cathode and Li metal as a counter electrode. The cells were first activated at a low current density, 28 mA g^{-1} (corresponding to 0.1 C-rate), and they were then cycled at a current density of 140 mA g^{-1} (corresponding to 0.5 C-rate) at 25 and 55 °C. The $Li[Ni_{0.8}Co_{0.2}]O_2$ electrode showed a high discharge capacity of 200 mAh g^{-1} at 25 °C and 205 mAh g^{-1} at 55°C (**Figure 6**a). The discharge capacity of the SSP $Li[Ni_{0.8}Co_{0.06}Mn_{0.14}]O_2$ electrode is higher than those of the $Li[Ni_{0.8}Co_{0.2}]O_2$ and bulk $Li[Ni_{0.8}Co_{0.06}Mn_{0.14}]O_2$ electrodes,

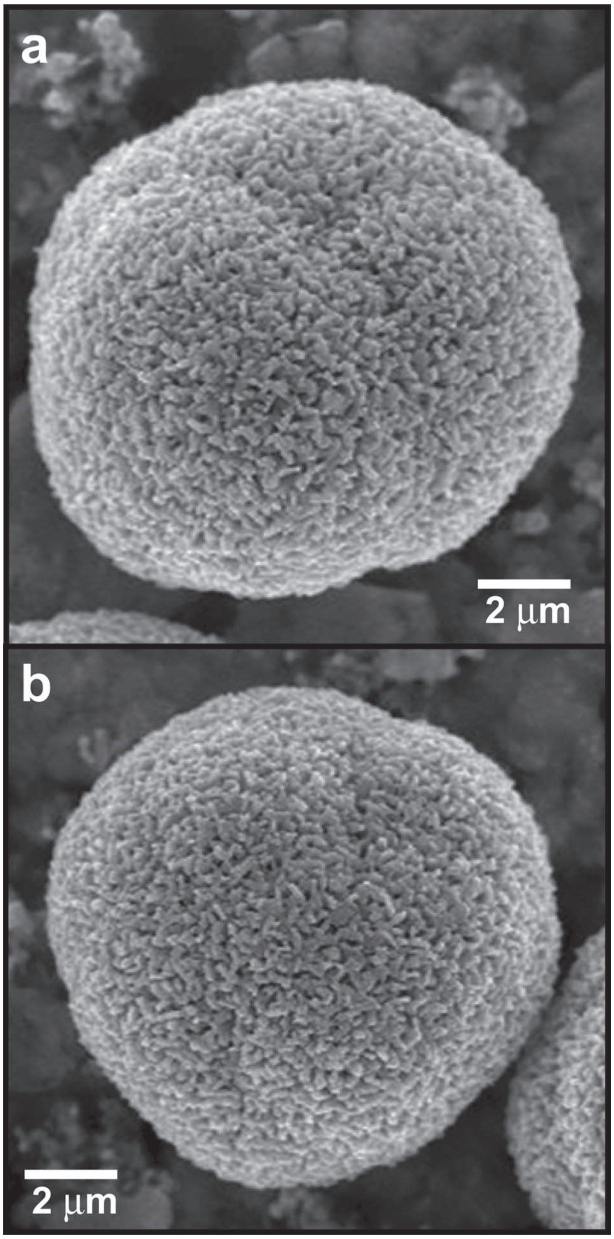

Figure 5. SEM images of the as-synthesized a) Li[$Ni_{0.8}Co_{0.2}$]O_2 and b) SSP Li[$Ni_{0.8}Co_{0.06}Mn_{0.14}$]$O_2$.

210 mAh g^{-1} (25 °C) and 215 mAh g^{-1} (55 °C). Interestingly, the operating voltages during charge and discharge were approximately 0.1 V higher for the SSP Li[$Ni_{0.8}Co_{0.06}Mn_{0.14}$]$O_2$ electrode, resulting in increased energy density. This phenomenon may be due to the presence of tetravalent Mn in the surface of the SSP Li[$Ni_{0.8}Co_{0.06}Mn_{0.14}$]$O_2$ electrode. In other words, the operation voltage of the Li[$Ni_{0.5}Mn_{0.5}$]O_2 electrode is higher than that of the Li[$Ni_{1/3}Co_{1/3}Mn_{1/3}$]O_2 electrode due to more tetravalent Mn in the crystal structure.[6,7,11,12,17] Thermodynamically, the presence of tetravalent Mn stabilizes the crystal structure further by increasing the bond strength between Mn and O, so that more energy is necessary to intercalate Li^+ into the structure, raising the operation voltage. A similar example is $LiFePO_4$, in which the $Fe^{2+/3+}$ redox potential is about 3.5 V vs. Li/Li^+.[18–20]

The capacity retention of Li[$Ni_{0.8}Co_{0.2}$]O_2 and SSP Li[$Ni_{0.8}Co_{0.06}Mn_{0.14}$]$O_2$ electrodes over 100 cycles is illustrated in Figure 6b. As expected, the Li[$Ni_{0.8}Co_{0.2}$]O_2 electrode exhibited disappointing cycling at 25 and 55°C. The capacity retention at the 100th cycle was found to be 53% at 25 °C and 48% at 55 °C. By contrast, the SSP Li[$Ni_{0.8}Co_{0.06}Mn_{0.14}$]$O_2$ electrode gives significantly improved capacity retention after 100 cycles: 87% at 25 °C and 81.4% at 55 °C, again which the propety is much better than that of the bulk Li[$Ni_{0.8}Co_{0.06}Mn_{0.14}$]$O_2$ electrode at both operation temperatures. Derivatives of the charge and discharge curves provide valuable insight into the electrochemical reactions that occurred during cycling. Such data obtained at 55 °C are depicted in Figure 6c,d. Voltage decay and shortening of the voltage plateau are evident for the Li[$Ni_{0.8}Co_{0.2}$]O_2 electrode (Figure 6c), whereas the operation voltage and plateau length were fairly constant upon cycling the SSP Li[$Ni_{0.8}Co_{0.06}Mn_{0.14}$]$O_2$ electrode (Figure 6d).

2.3. Analysis of Post-Cycling Electrodes

The XRD patterns for the extensively cycled electrodes were compared to those of the as-synthesized Li[$Ni_{0.8}Co_{0.2}$]O_2 and SSP Li[$Ni_{0.8}Co_{0.06}Mn_{0.14}$]$O_2$ electrodes; the XRD pattern of the Al current collector was used as an internal standard for calibration purposes. A striking feature for the Li[$Ni_{0.8}Co_{0.2}$]O_2 after cycling is that the peaks shifted toward lower 2θ compared with the as-synthesized electrodes (**Figure 7**a), and the diffraction peaks became quite broad, particularly the (113) peak. Also, a clear split of (006)/(102) peaks was observed after cycling. Measurement of cation mixing was not possible for the extensively cycled electrodes from the XRD patterns shown in Figure 7a due to the severe deformation of the peaks, indicating low reliability. For the SSP Li[$Ni_{0.8}Co_{0.06}Mn_{0.14}$]$O_2$, on the contrary, peak splitting and broadening of diffraction peaks were not observed (Figure 7b). Lattice parameters calculated by the least square method are shown in **Table 3**. It is evident from these data that the Li[$Ni_{0.8}Co_{0.2}$]O_2 underwent a dramatic change in the lattice parameters; comparing the as-synthesized with the cycled Li[$Ni_{0.8}Co_{0.2}$]O_2, the difference in the *a*-axis is 0.03–0.04 Å for both 25 °C and 55 °C cycling, and the difference in the *c*-axis is 0.19-0.20 Å for 25 °C and 55 °C cycling. Interestingly, the calculated lattice structure for the cycled SSP Li[$Ni_{0.8}Co_{0.06}Mn_{0.14}$]$O_2$ did not undergo the serious deformation that occurred for the Li[$Ni_{0.8}Co_{0.2}$]O_2 electrode. The lattice varied less than 0.01 Å in the *a*-axis and 0.06 Å in the *c*-axis after the extensive cycling at 25 °C and 55 °C. From thermodynamic considerations, the Gibbs energy of formation at 298 K for tetravalent Mn in MnO_2 (–465.2 kJ mol^{-1}) is much lower than that of NiO (–211.7 kJ mol^{-1}),[21] and we thus are able to hypothesize that the formation of tetravalent Mn in the surface region of the solid solution particle fosters the structural stabilization. As we postulated on the basis of Figure 1, the formation of solid-solution Li[$Ni_{0.8}Co_{0.1}Mn_{0.1}$]O_2-Li[$Ni_{0.8}Co_{0.02}Mn_{0.18}$]$O_2$ in a particle, which is coordinated with tetravalent Mn in the surface, stabilizes the crystal structure, and this stabilization successfully maintains the high capacity and structural integrity upon cycling.

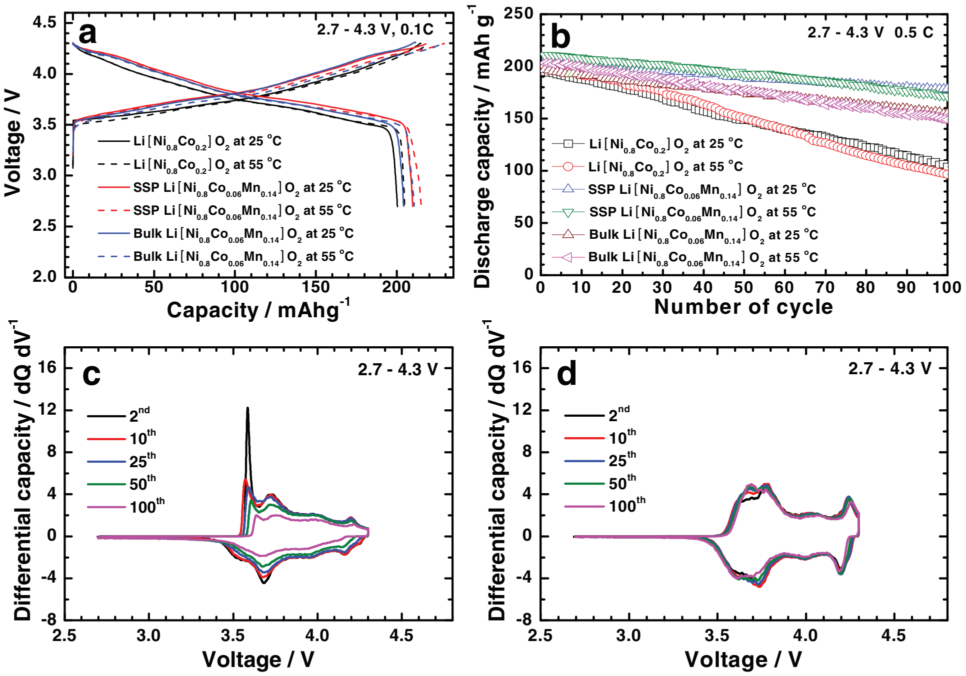

Figure 6. a) First charge and discharge curves of Li/Li[$Ni_{0.8}Co_{0.2}$]O_2 cell, Li/bulk Li[$Ni_{0.8}Co_{0.06}Mn_{0.14}$]$O_2$ cell, and Li/SSP Li[$Ni_{0.8}Co_{0.06}Mn_{0.14}$]$O_2$ cell operated at 25 °C and 55 °C. b) Capacity retention of Li/Li[$Ni_{0.8}Co_{0.2}$]O_2 cell, Li/bulk Li[$Ni_{0.8}Co_{0.06}Mn_{0.14}$]$O_2$ cell, and Li/SSP Li[$Ni_{0.8}Co_{0.06}Mn_{0.14}$]$O_2$ cell operated at 25 °C and 55 °C. c,d) Derivative curves during 100 cycles measured at 55 °C for Li[$Ni_{0.8}Co_{0.2}$]O_2 (c) and SSP Li[$Ni_{0.8}Co_{0.06}Mn_{0.14}$]$O_2$ (d).

2.4. Thermal Properties

We performed thermogravimetric analysis (TGA) and high-temperature in situ XRD of the chemically delithiated $Li_{0.1}[Ni_{0.8}Co_{0.2}]O_2$ (mixture phases of $P\bar{3}m1$ and $R\bar{3}m$) and SSP $Li_{0.1}[Ni_{0.8}Co_{0.06}Mn_{0.14}]O_2$ ($P\bar{3}m1$). Three distinct features were observed in the TGA curves (**Figure 8**) for the $Li_{0.1}[Ni_{0.8}Co_{0.2}]O_2$ on heating from 50 °C to 600 °C: i) 50–160 °C (1.5% weight loss), ii) 160–260 °C (11.6% weight loss), and iii) 260–600 °C (11.8% weight loss). The total of 24.9% weight loss is ascribed to the evaporation of oxygen from the crystal lattice. In the temperature range of 50–160 °C, the weight loss remained unchanged to 130 °C, though the relative diffraction intensity decreased (**Figure 9**a,b), indicating structural reordering to form a new phase. At 150 °C, the main peaks of $P\bar{3}m1$ phase and $R\bar{3}m$ phase merged, and a new spinel phase, M_3O_4 (M = Ni and Co, *Fd3m*), formed at 160 °C (Figure 9b). Meanwhile, a cubic phase of NiO (*Fm3m*) also developed, although the majority of the phases were composed of the spinel phase (Figure 9a). In the second temperature range (160–260 °C), the relative intensity of the cubic spinel phase became weaker as the temperature increased, which is also evidenced from the (111) peak shown in Figure 9b. Finally, the spinel phase was extinguished at 260 °C. In this region, the evaporated oxygen from the crystal structure corresponds to 11.6% in total weight. The drastic loss of oxygen in the structure likely facilitates the structural rearrangement, giving single-phase NiO. In the third temperature range (260–600 °C), the weight was lost linearly with increasing temperature. The resulting crystallinity of the cubic NiO phase gradually improved with temperature. The formed cubic NiO phase was retained after cooling to 25 °C.

For the chemically delithiated SSP $Li_{0.1}[Ni_{0.8}Co_{0.06}Mn_{0.14}]O_2$, different thermal behavior was observed (Figure 8). It exhibited four steps of weight loss during heating to 600 °C: i) 50–190 °C (0.5% weight loss), ii) 190–260 °C (6.5% weight loss), iii) 260–370 °C (8.4% weight loss), and iv) 370–600 °C (5.8% weight loss). The weight loss was very small in the first temperature range, where the original structure of $P\bar{3}m1$ was maintained to 180 °C. An O1 type layer structure ($P\bar{3}m1$) was transformed to cubic spinel M_3O_4 phase (M = Ni, Co and Mn) at 190 °C (Figure 9c,d). Similar to the $Li_{0.1}[Ni_{0.8}Co_{0.2}]O_2$, the cubic NiO phase was observed as soon as the cubic spinel phase was formed. This spinel phase was seen up to 260 °C, when 6.5% oxygen was evaporated from the structure, after which the thermal behavior was similar to that of the $Li_{0.1}[Ni_{0.8}Co_{0.2}]O_2$ to 600 °C (Figure 9c), although the chemically delithiated SSP $Li_{0.1}[Ni_{0.8}Co_{0.06}Mn_{0.14}]O_2$ exhibited more complicated thermal decomposition in the TGA curves. The extinction temperature for the spinel phase was the same for both delithiated compounds, 260 °C. The only difference in the thermal behavior was the formation temperature of the spinel phase: this temperature was delayed to 190 °C for the SSP $Li_{0.1}[Ni_{0.8}Co_{0.06}Mn_{0.14}]O_2$, which has tetravalent Mn in the surface. We attribute this higher temperature of the phase transformation to the presence of a stronger bond of Mn^{4+}-O in the surface requiring more energy to rearrange the structure to cubic spinel phase. As a result, a much reduced amount of oxygen was released from the structure in the TGA temperature range compared with that of the $Li_{0.1}[Ni_{0.8}Co_{0.2}]O_2$.

Next, the thermal properties of electrochemically delithiated wet electrodes of $Li_{0.23}[Ni_{0.8}Co_{0.2}]O_2$ and SSP $Li_{0.22}[Ni_{0.8}Co_{0.06}Mn_{0.14}]O_2$ were examined by differential scanning calorimetry (DSC) (see **Figure 10**). As expected from the XRD studies (Figure 9),

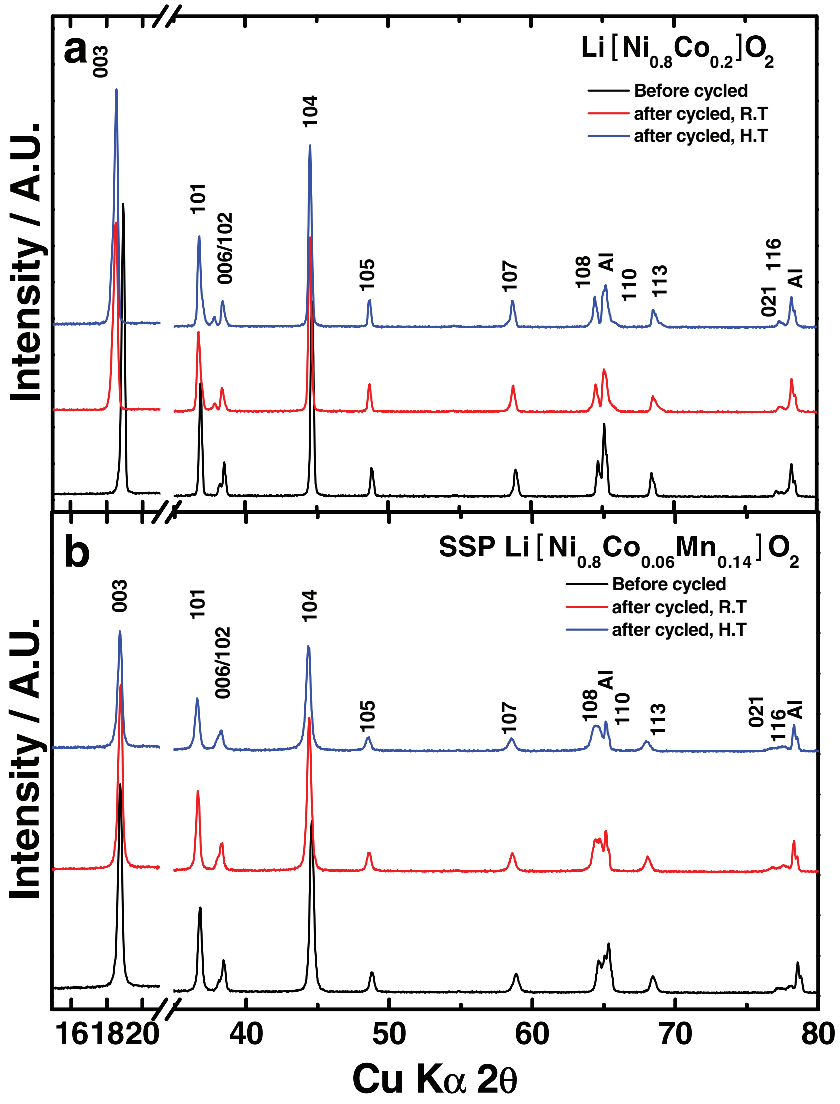

Figure 7. XRD patterns of the as-synthesized electrode and extensively cycled a) Li[$Ni_{0.8}Co_{0.2}$]O_2 and b) SSP Li[$Ni_{0.8}Co_{0.06}Mn_{0.14}$]$O_2$ electrodes at 25 °C and 55 °C.

the onset exothermic reaction took place at 150 °C for the $Li_{0.23}$[$Ni_{0.8}Co_{0.2}$]O_2 electrode, initiating the phase transformation to the cubic spinel phase. The main exothermic reaction occurred at 230 °C with approximately 984 J g^{-1} of heat due to the drastic evaporation of oxygen from the crystal structure, leading to rearrangement of the structure. The exothermic reaction terminated at around 270 °C, indicating the end of the phase transformation to cubic NiO phase. By contrast, the onset temperature of the exothermic reaction began at around 200 °C for the SSP $Li_{0.22}$[$Ni_{0.8}Co_{0.06}Mn_{0.14}$]$O_2$ electrode, and the main exothermic reaction appeared at 250 °C. These results again confirm that the presence of tetravalent Mn in the surface delays the phase transformation and results in less evolution of oxygen from the structure due to the stronger Mn^{4+}-O bond in the surface. The heat generation was approximately 810 J g^{-1} for the SSP $Li_{0.22}$[$Ni_{0.8}Co_{0.06}Mn_{0.14}$]$O_2$ electrode, which is much smaller than that of the $Li_{0.23}$[$Ni_{0.8}Co_{0.2}$]O_2 electrode.

3. Conclusions

Nickel-rich Li[$Ni_{1-x}M_x$]O_2 (M = Ni, Co, and Mn) is an attractive cathode material due to its high capacity in the moderate voltage range. For vehicle applications, a high capacity material with high energy density is greatly desirable because the mounting space for the battery pack is tightly limited. So far, interest in this material as a cathode has been limited due to its poor thermal properties at the highly delithiated state. As we hypothesized, the formation of a continuous SSP of Li[$Ni_{0.8}Co_{0.1}Mn_{0.1}$]O_2–Li[$Ni_{0.8}Co_{0.02}Mn_{0.18}$]$O_2$, which has an average composition of Li[$Ni_{0.8}Co_{0.06}Mn_{0.14}$]$O_2$, suggests that the Ni-rich Li[$Ni_{1-x}M_x$]O_2 system should be considered again for vehicle applications. With the presence of tetravalent Mn in the surface, the Ni-rich SSP Li[$Ni_{0.8}Co_{0.06}Mn_{0.14}$]$O_2$ electrode could realize high capacity, long life and lower soluability in the electrolyte as well, and desirable thermal properties that have never been achieved in Ni-rich Li[$Ni_{1-x}M_x$]O_2.

Table 3. Comparison of lattice parameters before and after the extensive cycling.

	Li[$Ni_{0.8}Co_{0.2}$]O_2		SSP Li[$Ni_{0.8}Co_{0.06}Mn_{0.14}$]$O_2$	
	a-axis [Å]	*c*-axis [Å]	*a*-axis [Å]	*c*-axis [Å]
Before cycling	2.8633	14.1602	2.8737	14.2129
After cycling at 25 °C	2.8975	14.3559	2.8793	14.2777
After cycling at 55 °C	2.9058	14.3624	2.8813	14.2791

4. Experimental Section

Synthesis: [$Ni_{0.8}Co_{0.2}$]$(OH)_2$ and [$Ni_{0.8}Co_{0.06}Mn_{0.14}$]$(OH)_2$ compounds were synthesized by the co-precipitation method. Appropriate amounts of $NiSO_4 \cdot 6H_2O$ and $CoSO_4 \cdot 7H_2O$ (cationic ratio of Ni:Co = 8:2) were used as the starting materials for [$Ni_{0.8}Co_{0.2}$]$(OH)_2$. The required amounts of starting materials were pumped continuously into a stirred tank reactor (CSTR, capacity 4 L) under a nitrogen atmosphere. At the same time, a 2.0 mol dm^{-3} solution (aq.) of NaOH and the desired amount of NH_4OH solution (aq.) (chelating agent) were also separately pumped into the reactor. The concentration, pH, temperature, and stirring speed of the reaction mixture were carefully controlled in the CSTR.

For the Ni-fixed full gradient structure formation of [$Ni_{0.8}Co_{0.2}$]$(OH)_2$ inner particles, Co-free aqueous solution was prepared by mixing required amounts of $NiSO_4$ and $MnSO_4$ salt solutions (Ni:Mn = 0.8:0.2 in molar ratio) and Mn-free (Ni:Co = 0.8:0.2 in molar ratio) solution separately. Initially, Co-free aqueous solution was slowly pumped into the stoichiometric amount of Mn-free solution, and at the same time, the homogeneously mixed solution, containing Ni, Co, and Mn ions, was fed into the CSTR. After a certain reaction time, green Ni-fixed full

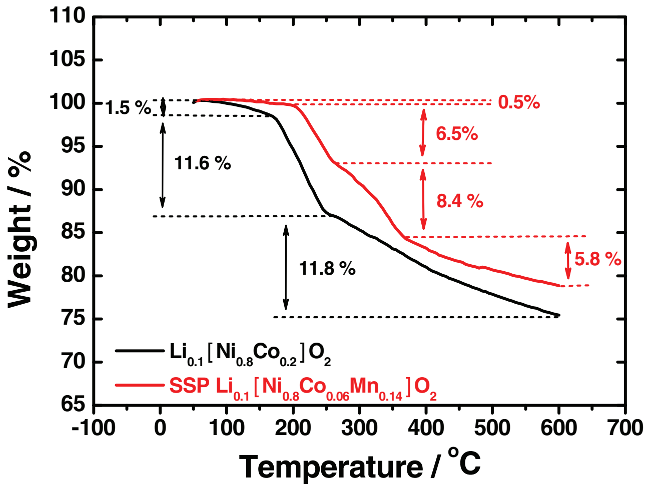

Figure 8. TGA curves of the chemically delithiated $Li_{0.1}[Ni_{0.8}Co_{0.2}]O_2$ and SSP $Li_{0.1}[Ni_{0.8}Co_{0.06}Mn_{0.14}]O_2$.

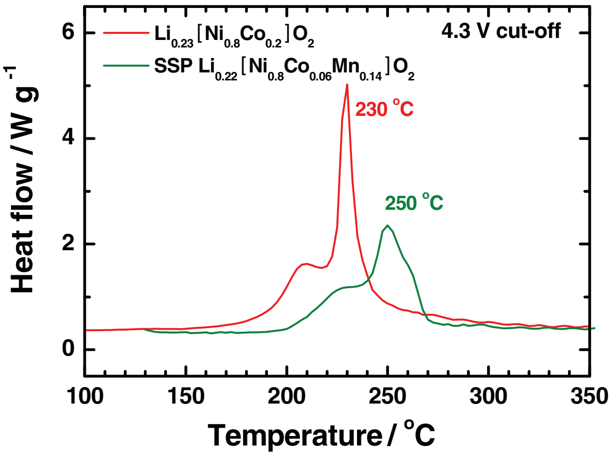

Figure 10. DSC curves of the electrochemically delithiated (charged to 4.3 V) $Li_{0.23}[Ni_{0.8}Co_{0.2}]O_2$ and SSP $Li_{0.22}[Ni_{0.8}Co_{0.06}Mn_{0.14}]O_2$ electrodes.

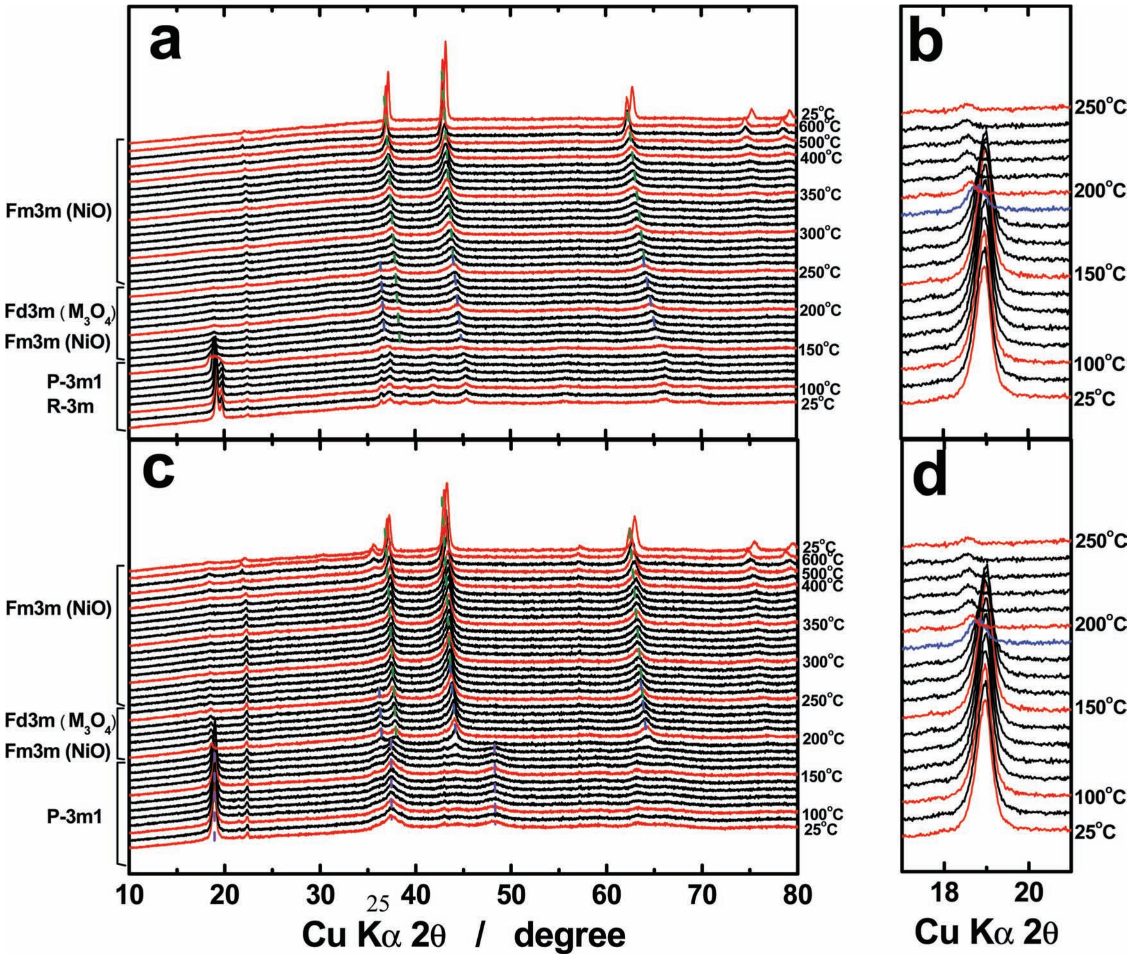

Figure 9. High-temperature in-situ XRD patterns of the a) chemically delithiated $Li_{0.1}[Ni_{0.8}Co_{0.2}]O_2$ and b) its magnified patterns in temperature range of 25–250 °C (blue line appearing at 160 °C indicates the formation of cubic spinel M_3O_4 phase). c) Chemically delithiated SSP $Li[Ni_{0.8}Co_{0.06}Mn_{0.14}]O_2$ and d) its magnified patterns in temperature range of 25–250 °C (blue line appearing at 190 °C indicates the formation of cubic spinel M_3O_4 phase).

gradient particles slowly accumulated. The co-precipitated precursor powders were filtered, washed, and dried at 110 °C.

These $[Ni_{0.8}Co_{0.2}](OH)_2$ and $[Ni_{0.8}Co_{0.06}Mn_{0.14}](OH)_2$ compounds were thoroughly mixed with $LiOH{\cdot}H_2O$ and heated at 750 °C for 10 h in air, respectively. The chemical compositions of the resulting powders were determined by atomic absorption spectroscopy (AAS, Vario 6, Analyticjena).

Physical Analysis: The morphology of the powders was determined with scanning electron microscopy (SEM, S-4800, Hitachi). Cross sections for SEM analysis were prepared by embedding the as-synthesized particles in an epoxy and polishing them flat on sand paper. Line scans for the full-gradient materials were obtained with an electron probe X-ray microanalyzer (EPMA, JXA-8100, JEOL). Powder X-ray diffraction (XRD, Rint-2000, Rigaku) measurements using Cu–Kα radiation were employed to identify the crystalline phase of the synthesized materials. The XRD data were obtained at $2\theta = 10$–$80°$, with a step size of 0.03° and a count time of 5 s. The collected intensity data from the XRD were analyzed by the Rietveld refinement program, Fullprof 2002.[22] For post-cycled electrodes, the lattice parameters were calculated by a least-squares method. X-ray photoelectron spectroscopy (XPS, PHI 5600, Perkin Elmer) measurements were made to investigate the electronic state of Ni, Co, and Mn for the concentration-gradient material. Macromode (about 3 mm × 3 mm) Ar^+ etching was used to determine the concentration depth profiles of the powders. The etching rate was estimated as 4.2 nm min^{-1}. Binding energies of XPS peaks of standards were referred to literature values.[23]

Electrochemistry: The electrochemical performance of the synthesized cathodes was assessed in R2032 coin-type cell. The cell consisted of a cathode and a lithium metal anode separated by a porous polypropylene film. The cathode was fabricated with a mixture of prepared powder (85 wt%), carbon black (7.5 wt%), and polyvinylidene fluoride (7.5 wt%) in *N*-methyl-2-pyrrolidone. The slurry was spread onto aluminum foil and dried in a vacuum oven at 110 °C. The electrolyte used was 1 M $LiPF_6$ in a 1:1 volume mixture of ethylene carbonate and diethyl carbonate (PANAX ETEC Co., Ltd).

Thermal Analysis: Chemical extraction of lithium from the synthesized materials was carried out by NO_2BF_4 (2-fold excess versus active material) in acetonitrile for several days under an Ar atmosphere in a glovebox. The reacted products were washed several times with acetonitrile to remove $LiBF_4$ and dried under Ar. The chemical compositions of the resulting powders were determined by atomic absorption spectroscopy. The chemically delithiated powders were subjected to thermogravimetric analysis (loaded sample amount: 10 mg, DTG-60, SHIMADZU) combined with in-situ high-temperature XRD (Rint-2200 and PTC-30, Rigaku). The high-temperature XRD (HT-XRD, X'Pert PRO MPD System, PANanalytical) patterns were collected on a Pt heating strip in air. For the thermogravimetric analysis, samples were thermally cycled from room temperature to 600 °C at a heating and cooling rate of 1 °C min^{-1} and were held at selected temperatures for 10 min prior to data collection. The XRD data were obtained at $2\theta = 10$–$80°$, with a step size of 0.03° and a count time of 0.5 s during each temperature increment.

For DSC experiments, cells were charged to 4.3 V and opened in an Ar-filled dry box. Samples of 3–5 mg were collected in a stainless steel sealed pan with a capacity of 30 μL and a gold-plated copper seal capable of withstanding 150 atm pressure. Thermal stability was determined in a differential scanning calorimeter (DSC, 200PC, Netzsch) using a temperature scan rate of 1 °C min^{-1}. The weight was constant in all cases, indicating that no leaks occurred during the experiments.

Acknowledgements

H.-J.N. and S.-T.M. contributed equally to this work. This work was supported by the Human Resources Development of the Korea Institute of Energy Technology Evaluation and Planning (KETEP) grant funded by the Korea government Ministry of Knowledge Economy (No. 20104010100560) and the National Research Foundation of Korea (NRF) grant funded by the Korea government (MEST) (No. 2009-0092780)

Received: March 13, 2012
Revised: May 1, 2012

[1] J. M. Tarascon, M. Armand, *Nature* **2001**, *414*, 359.
[2] S.-U. Woo, B.-C. Park, C. S. Yoon, S.-T. Myung, J. Prakash, Y.-K. Sun, *J. Electrochem. Soc.* **2007**, *154*, A649.
[3] H. Arai, S. Okada, Y. Sakurai, J. Yamaki, *Solid State Ionics* **1998**, *109*, 295.
[4] Y. E. Hyung, D. R. Vissers, K. Amine, *J. Power Sources.* **2003**, *191–121*, 383.
[5] Y. Abu-Lebdeh, I. Davidson, *J. Power Sources* **2009**, *189*, 576.
[6] T. Ohzuku, Y. Makimura, *Chem. Lett.* **2001**, *30*, 642.
[7] Z. Lu, D. D. MacNeil, J. R. Dahn, *Electrochem. Solid-State Lett.* **2001**, *4*, A191.
[8] Y.-K. Sun, S.-T. Myung, M.-H. Kim, J. Prakash, K. Amine, *J. Am. Chem. Soc.* **2005**, *127*, 13411.
[9] Y.-K. Sun, S.-T. Myung, B.-C. Park, J. Prakash, I. Belharouak, K. Amine, *Nat. Mater.* **2009**, *8*, 320.
[10] Y.-K. Sun, D.-H. Kim, C. S. Yoon, S.-T. Myung, J. Prakash, K. Amine, *Adv. Funct. Mater.* **2010**, *20*, 485.
[11] Y.-K. Sun, S.-T. Myung, H. J. Bang, B.-C. Bang, S.-J. Park, N.-Y. Sung, *J. Electrochem. Soc.* **2007**, *154*, A937.
[12] K.-S. Lee, S.-T. Myung, K. Amine, H. Yashiro, H.-K. Sun, *J. Electrochem. Soc.* **2007**, *154*, A971.
[13] R. D. Shannon, *Acta Crystallogr., Sect. A: Cryst. Phys., Diffr., Theor. Gen. Crystallogr.* **1976**, *32*, 751.
[14] M.-H. Lee, Y.-J. Kang, S.-T. Myung, Y.-K. Sun, *Electrochim. Acta* **2004**, *50*, 939.
[15] K.-S. Lee, S.-T. Myung, J.-S. Moon, Y.-K. Sun, *Electrochim. Acta* **2008**, *53*, 6033.
[16] S.-T. Myung, M.-H. Lee, S. Komaba, N. Kumagai, Y.-K. Sun, *Electrochim. Acta* **2005**, *50*, 4800.
[17] T. Ohzuku, Y. Makimura, *Chem. Lett.* **2001**, *30*, 744.
[18] A. K. Padhi, K. S. Nanjundaswamy, J. B. Goodenough, *J. Electrochem. Soc.* **1997**, *144*, 1188.
[19] J. B. Goodenough, *Solid State Ionics.* **1994**, *69*, 184.
[20] A. Manthiram, J. B. Goodenough, *J. Solid State Chem.* **1987**, *71*, 349.
[21] J. A. Dean, *Lange's Handbook of Chemistry*, 4th ed., McGraw-Hill Inc., New York **1992**, p. 6.81.
[22] T. Roisnel, J. Rodriguez-Carjaval, *Fullprof Manual*, Institut Laue-Langevin, Grenoble **2002.**
[23] C. D. Wagner, W. M. Riggs, L. E. Davis, J. F. Moulder, *Handbook of X-Ray Photoelectron Spectroscopy*, PerkinElmer Corp., Physics and Electronics Division, Eden Prairie, MN **1979**.